COURSE ON 3-D MORPHOLOGICAL OPERATORS

Jean Serra
Centre de Morphologie Mathématique
École Nationale Supérieure des Mines de Paris
35, rue Saint-Honoré
77305 Fontainebleau Cedex FRANCE
serra@cmm.ensmp.fr

8th *European Congress for Stereology and Image Analysis*
University of Bordeaux 1, FRANCE
September 4-7, 2001

Contents

Chapter 1

3-D Structures and Operations

1.1 Introduction

In image processing, 3-D treatments appeared during the 80's for both analysis and synthesis purposes. In the present paper, we concentrate on analysis of images, or more precisely, of stacks of binary images. These piles of sections are nowadays currently produced macroscopically (e.g. NMR), or at microscopical scales (e.g. confocal microscopes). They produce experimental data on 3-D rasters which tend to be cubic. Downstream, these computerized data are binarized by some techniques we will not consider here. These binary data constitute, by definition, sets in Z^3, as well as estimations of sets of R^3. How to access them ? How to extend to the 3-D space the usual 2-D notions of sizes, directions, distances, connectivity, homotopy, etc. ? This is what we would like to develop hereafter. What follows is basically a tutorial ; however the space graph approach for homotopy and decomposition of cube-octahedra are new results (as far as I know). A survey of literature shows that in 3D morphology, the two places that have been producing the most substantial series of results, and for a long time, are the pattern recognition section, at Delft University of Technology (see in particular P.W. Verbeek [35], J.C. Mullikin [22], Jonker [17]) and the Centre de Morphologie Mathématique, at the Ecole des Mines de Paris (see in particular Serra [26], Meyer [21] [12], Gratin [13], Gesbert et al.[11]).

1.2 Three dimensional grids

By grid, we do not only mean a regular distribution of points in the the 3-D space, but also a definition of the elementary edges, faces, and polyhedra associated with these points. The three crystallographic grids we find below derive from the cube, and are constructed as follows

i/ cubic grid, which is generated by translations of a unit cube made of 8 vertices ;

ii/ the centred cubic grid (cc grid) where the centres of the cubes are added to the vertices of the previous grid ;

iii/ the face-centred cubic grid (fcc grid) where the centres of the faces are added to the vertices of the cubic grid.

A comprehensive comparison of these grids can be found in F. Meyer's study [21].

1.2.1 Interplane distances

In the last two grids, the vertices generate square grids in the horizontal planes, and in vertical projection the vertices of plane No n occupy the centres of the squares in plane No $n-1$. We shall say that these horizontal plane are *staggered*. If a stands for the spacing between voxels in the horizontal planes, then the interplane vertical spacing is equal to $a/2$ in the cc case, and to $a\sqrt{2}/2$ in the fcc one.

1.2.2 First neighbors

Every vertex has

- 6 first neighbors in the cubic case
- 8 first neighbors in the cc case
- 12 first neighbors in the fcc case

Geometrically speaking, when point x is located at the centre of the $3 \times 3 \times 3$ cube, its projections

- on the faces of the cube provide the cubic neighbors
- on the vertices the cc-neighbors
- and on the edges the fcc-neighbors

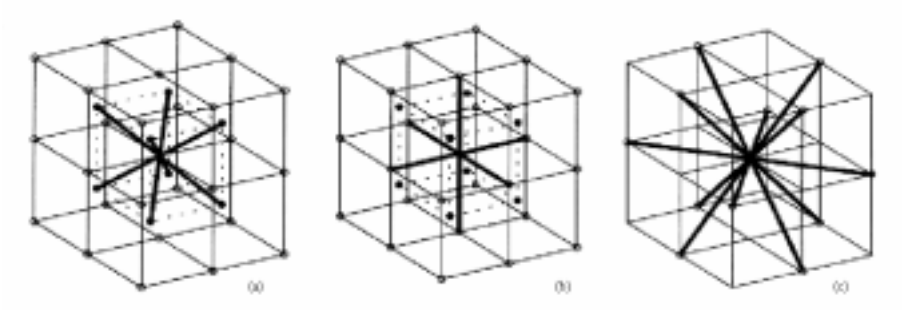

Figure 1.1: The three 3-D grids that derive from the cubic symmetry.

Fig. (1.1) illustrates this point. One can see, also, that the first neighbors generate the smallest isotropic centred polyhedron of the grid, i.e. a 7-voxel tetrahedron (cubic case) a 9-voxel cube (cc-grid) a 13-voxel cube-octahedron (fcc grid). Denote them by the generic symbol B, and the nth iteration of B by B_n, i.e.

$$B_n = B \oplus B \quad ... \quad \oplus B \qquad n \text{ times} \ ,$$

with $B_0 =$ Identity. From the implication $n \geq p \Rightarrow B_n \geq B_p \qquad n, p$ non negative integers, from the equality $B_n B_p = B_{n+p}$, and from the symmetry of B we draw (proposition 2.4 in Serra [29]) that the 3-D raster of points turns out to be a metric space (in three different ways, according to the grid), where the smallest isotropic centred polyhedron is the unit ball.

1.3 Elementary edges, faces, and polyhedra

In order to complete the definition of the grids, we will introduce now elementary edges, faces and polyhedra. Edges are necessary to define paths, hence connectivity. Faces and polyhedra are required to introduce notions such as Euler-Poincare number for example, or more generally, to introduce the graph approach.

1.3.1 Cubic grid

As elementary edges, the best candidates are obviously the closest neighbors (in the Euclidean sense), i.e. those of fig. (1.1). However, they are not so

numerous, in the cubic and in the cc case, in particular, which leads to poor connections. For example, in the cubic grid, the extremities of the various diagonals are not connected, we meet here a circumstance similar to that which led to the 8 and 4-connectivities in the 2-D grid. For the same reason, the authors who focused on the cubic grid, such as A. Rosenfeld [19], at the beginning of the 80's, introduced the 26- and the 6-connectivity on the cubic grid. When the foreground X is 26-connected, then the background X^c is 6-connected and vice-versa. In other words, a voxel $x \in X$ admits, as edge partners, all those voxels $y \in X$ that pertain to the cube $C : 3 \times 3 \times 3$ centred at x. Coming back to fig.(1.1b), we now have to take into account not only the centres of the cube faces, but also the 12 middle points of its edges, and its 8 vertices. Such an extension of the connectivity for X is possible only when the connectivity on X^c remains restricted to the six closest neighbors. If not, we should run the risk of over crossings of diagonals of $1's$ and of $0's$, so the faces should be undefined.This dissymmetrical connectivity brings into play a second digital metric, where cube $3 \times 3 \times 3$ is the unit ball. In particular, the boundary of set X^c is

$$\delta X^c = X^c \setminus X^c \ominus C$$

whereas the boundary of set X is defined via the unit tetrahedra T:

$$\delta X = X \setminus X \ominus C$$

We draw from this last equation that $\delta X \ominus T = \emptyset$, and from the previous one that $\delta X^c \ominus C = \emptyset$. The boundary of X is thinner, but it may comprise zones of a thickness 2, and of course lines or fine tubes.

Note also that, unlike tetrahedron T, cube C admits a Steiner decomposition into three orthogonal segments of three voxels length each. Consequently, the dilation $X \oplus nC$ is obtained as the product of three linear dilations of size $2n$ in the three directions of the grid.

1.3.2 cc grid

The cc grid call very similar comments, but now with staggered horizontal planes. The low number of the first neighbors (i.e. 8) of each voxel suggests to add the second neighbors, in number of six (see fig.1.1). This results in the unit rhombododecahedron R shown in fig.(1.2), which exhibits 15 vertices (including the centre), 12 rhomb faces, identical up to a rotation, and 24 edges whose common length is the first neighbor distance.

Just as previously, with the cubic grid, the adjunction of 2nd neighbors complicate the situation, for they cannot be added simultaneously to the $1's$ and $0's$. This results in a 14-connectivity for the grains versus a 8-connectivity for the pores. By comparison with the cubic case, the connectivity contrast between foreground and background is reduced, but it remains.

Again, as previously, a new metric is provided, namely that of the rhombododecahedron. In this metric, the isotropic dilations can be decomposed into segment dilations, since R admits a Steiner decomposition into the four diagonals of the cube $(2,2,2)$, i.e.

$$R = \begin{pmatrix} 1 & . \\ . & 0 \end{pmatrix} \oplus \begin{pmatrix} 0 & . \\ . & 1 \end{pmatrix} \oplus \begin{pmatrix} . & -1 \\ 0 & . \end{pmatrix} \oplus \begin{pmatrix} . & 0 \\ -1 & . \end{pmatrix} \tag{1.1}$$

where -1, 0, 1 indicate the level of the plane, and where the origin is always assigned to the point of plane 0 [10].

1.3.3 fcc grid

With the fcc grid, things become simpler [6][8]. We still are in a grid where the odd horizontal planes have been shifted by $(a/2, a/2, 0)$ from the cubic spacing, but now each voxel x admits 14 nearest neighbors, at a distance $a\sqrt{2}/2$. They form the unit cube-octahedron D, of figure (1.2), centred at point x. Geometrically speaking, such a high number of first neighbors means that the shape of D is a better approximation of the Euclidean sphere, than those of the cube C and the rhombododecahedron R.

As far as connections are concerned, it becomes cumbersome to resort to 2nd neighbors. Therefore there no longer is a risk of diagonal overcrossing. The existence of an edge no longer depends on the phase under study but exclusively on the intersection between grid and sets: two neighbors $1's$ define an edge in set X, two neighbors $0's$ an edge in set X^c.

Finally X and X^c are treated by the same balls D_n, but the latter cannot be decomposed into Minkowski sum of segments, unlike C and R.

1.3.4 Comparison of the grids

As a conclusion, three reasons argue in favor of the fcc grid, namely

1/ the shape of the cube-octahedron D provides a better approximation of the unit Euclidean sphere, than C or R (isotropic dilations, skeletons, distance functions, etc. will seem more "Euclidean") ;

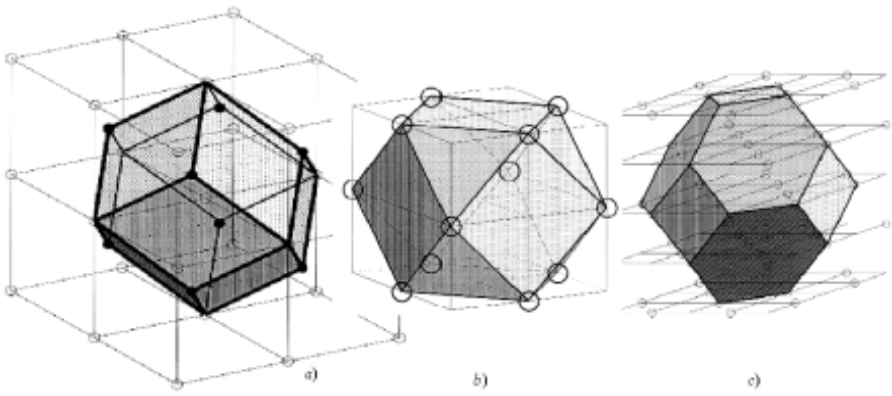

Figure 1.2: a): The rhombo-dodecahedron; b): The cube-octhedron; c) The tetrakai-decahedron.

2/ D is more condensed: 13 points on 3 consecutive planes (D) are more economic than 15 points on 5 planes (R), or 27 on 3 planes. D leads to thinner boundaries, to finer ultimate erosions, etc. and requires less logical tests in its implementation.

3/ In the fcc grid, the connectivity is based on the first neighbors only, which allows a common approach for grains and for pores (in cubic grid, when one decides to attribute *a priori* more than four possible neighbors to the $1's$ than to the $0's$, a rather severe assumption is made, which holds, paradoxically, on the convexity of the *pores*. Most often, both grains and pores exhibit concave and convex portions, and the 26/6-connectivity assumption is just irrelevant).

Facing these advantages, the weakness of the fcc grid is the staggered organization of its successive horizontal planes. However, is it really a drawback ? This is the question we will examine now.

1.4 Directions

In this section, we analyse how the directions, hence the shapes, are modified when embedding the digital 3-D grids into the Euclidean space. First of all a brief (and last) reminder on our three polyhedra is provided.

1.4.1 Equidistributed directions in R^3 and in Z^3

In R^2, we can subdivide the unit disc in as many equal arcs as we want. In R^3, unfortunately, such nice simplicity vanishes : given an arbitrary integer n, one cannot find in general n equidistributed directions on the unit sphere, i.e. one cannot partition this sphere into n solid angles which would derive from one another by rotations (a question related to the famous five Platonian polyhedra). Indeed, the 3-D space may be partitioned only into 2, 4, 6, 8, 12 and 20 equal solid angles. The first two partitions are too poor and the last one hardly reachable by small digital polyhedra. The partitions into 6, 8 and 12 angles are those seen from the centre of a cube, an octahedron and a rhombododecahedron respectively, whose faces are windows.

A second and less known result is the following. The axes of these 6, 8 and 12 solid angles coincide with the vectors from a voxel to its 6, 8 and 12 first neighbors in the cubic, cc and fcc grids respectively

These results directly extend to digital grids. For example, in the cubic grid, there are three sets of equi-angular directions, namely

i/ the three basic directions of the grid ;

ii/ the four directions involved in eq. 1, which are also the edges directions of the rhombododecahedron ;

iii/ the six following directions

$$\begin{pmatrix} 0 & 1 \\ . & . \end{pmatrix};\begin{pmatrix} 0 & -1 \\ . & . \end{pmatrix};\begin{pmatrix} 0 & . \\ 1 & . \end{pmatrix};\begin{pmatrix} 0 & . \\ -1 & . \end{pmatrix};\begin{pmatrix} . & 0 \\ 0 & . \end{pmatrix};\begin{pmatrix} 0 & . \\ . & 0 \end{pmatrix} \tag{1.2}$$

which correspond to the edge directions of the cube-octahedron.

Note that the dilation of the first three unit vectors (i) generate the unit cube ($2\times2\times2$), that of the four ones (ii) produces the rhombododecahedron (cf. Eq. 1.1), and that of the six vectors of (Eq. 1.2) the tetrakaidecahedron (but not the cube-octahedron...). In addition, each of these three Steiner polyhedra generates by translation a partition of the 3-D space R^3 or Z^3. The tetrakaidecahedron (fig. 1.2), a sort of Steiner version of the cube-octahedron, is unfortunately too thick for digital purposes (voxels distributed over five successive planes for the unit size).

As for the cube-octahedron itself, if it cannot be obtained by dilating segments, it admits, however, a decomposition into the Minkowski sum of two tetrahedra. For example

$$\begin{matrix} 0 & 1,-1 & 0 \\ 1,-1 & 0 & 1,-1 \\ 0 & 1,-1 & 0 \end{matrix} = \begin{pmatrix} 0 & -1 \\ -1 & 0 \end{pmatrix} \oplus \begin{pmatrix} 0 & +1 \\ +1 & 0 \end{pmatrix} \tag{1.3}$$

1.4.2 Digital fcc grids, virtual staggering

How to produce a stack of staggered square grids, or, equivalently, how to produce a digital unit cube-octahedron ? An easy way is to favor the diagonal horizontal directions, as in Eq. 1.3. The staggering structure is created automatically, since each of the two diagonal subgrid appears, alternatively, in the successive horizontal planes. The negative counterpart is that half of the voxels only are taken into account. For example, the dilation of Eq. 1.3 produces neither the central points at levels +1 and -1, nor the middle points of the sides at level zero. We may always add these points, in order to complete the basic cube-octahedron, but then

i/ We increase the elementary size from 13 up to 19 voxels, hence we become less accurate in delineating boundaries, ultimate erosions, skeletons, etc.

ii/ We lose the advantage of a unique type of edges, which governs homotopy and connectedness properties.

iii/ We do not know what to do with the amount of information carried by the non used voxels.

An alternative solution should consist in interpolating one horizontal grid every two planes. This would add a computational step, but above all, it seems "fiddled": how to weight the four horizontal neighbors, versus the two vertical ones ? How to display the resulting grid ? etc. Therefore, we propose neither to move nor to remove or even modify, any voxel of the cubic initial data, and to consider each even plane, *as it is*, as being staggered. According as the central plane is odd or even, we then obtain one of the two elementary polyhedra of fig. 1.3.

Such a *virtual staggering* is similar to that used in $\mathbb{Z}^2$, when one generates a hexagonal grid from a square raster. In both cases, the irregularity of the unit polyhedron (resp. polygon) is self-compensated by iteration. In other words, the mappings which bring into play sequences of successive sizes, such as distance functions, medial axes, granulometries, sequential alternated filters, etc. are treated by means of *actual* digital cube-octahedra (resp. hexagons), (see fig. 1.5).

1.5 Space graphs and measurements

From now on, we consider sets of points in $\mathbb{Z}^3$, that model the voxels associated with physical objects of the three dimensional space. Sets are given

$$\textit{upper and lower planes}\begin{pmatrix}1&1&.\\1&1&.\\.&.&.\end{pmatrix}\quad \textit{central plane}\begin{pmatrix}.&1&.\\1&1&1\\.&1&.\end{pmatrix}\quad a)$$

$$\textit{upper and lower planes}\begin{pmatrix}.&.&.\\.&1&1\\.&1&1\end{pmatrix}\quad \textit{central plane}\begin{pmatrix}.&1&.\\1&1&1\\.&1&.\end{pmatrix}\quad b)$$

Figure 1.3: Decomposition of the unit cube-octahedron on the cubic grid in order to simulate the staggered structure (a: odd central plane, b: even central plane).

capital letters (X, A, B...), and points small letters.

One find a rather important literature on digital surface description, and calculus, for 3-D sets [19][23][22]. If one has in mind to bridge the gap between digital and continuous spaces, i.e. to provide a Euclidean meaning with digital measurements, the techniques based on digital boundary measurement (i.e. volume difference between dilate and object, or object and eroded set) are not sufficient, and one must deal with stereology [4][11][15][21]. Below we follow this approach. Moreover we are not exclusively interested in surface area, but more generally in digital estimators of "good" Euclidean measurements.

1.5.1 Reminder on the genus of a surface

The theory of Euclidean surfaces is classical, and dates back to the beginning of the 20th century (R. Poincaré). The comment below derives from [16], more information can be found in general documents such as Encyclopedia Britannica.

In R^n, a *closed orientable surface* is topologically equivalent to a sphere with an even number $2p$ of holes (made by removing discs) which have been connected in pairs by p *handles* (shaped like the surface of half of a doughnut). A *closed non orientable surface* is topologically equivalent to a sphere which has had a certain number q of discs replaced by *cross-caps*. The numbers p and q are said to be the genus of the surface not being closed means that some discs have been removed and the hole left open. A torus is a sphere with one handle ; a Möbius strip is a sphere with one cross-cap and one "hole" ; a Klein bottle is a sphere with two cross-caps ; a cylinder is a

sphere with two "holes". In general, the Euler-Poincaré number of a surface is equal to $2-2p-q-r$, where p is the number of handles, q is the number of cross-caps (zero for an orientable surface), and r is the number of holes (or boundary curves). The Euler Poincaré number of the union of disjoint surfaces is the sum of each of them.

1.5.2 Euler-Poincaré number and space graphs

Historically, the Euler-Poincaré constant (in brief:EPC) appeared in two slightly different domains of mathematics. Firstly, there was Euler's reasoning about the relations between the polyhedrons vertices, edges and faces, which was formalized in terms of planar graphs by Cauchy. This way of thinking leads to counting algorithms, which are based on the elementary edges, squares and triangles (in the hexagonal grid). It extends to various cubic, cube-octahedron and rhombo-dodecahedron of R^3, without any particular theoretical difficulty, but with a growing heaviness of the elementary operations to be carried out.

The second way, Poincaré's, and Hadwiger's later on, links the successive definitions of EPC thanks to an induction holding on the dimensions of the space [14]. When transposed to a digital grid, this approach is limited to cubic (or to parallelepipedic) grids, but, in return, leads to a much simpler and faster expression than the graphs one. Thus, for a bounded digital set A, we have :

In Z^1, $v_1(A) = N(\text{vertices}) - N(\text{edges}) = N(\bullet) - N(-)$

In Z^2, for the square grid :

$$\begin{aligned} v_2(A) &= N(\text{vertices}) - N(\text{edges}) + N(\text{faces}) \\ &= N(\bullet) - N(-) - N(|) + N(\square) \end{aligned}$$

Still in Z^2, if we agree on calling $N_1(A)$ the sum of the constants $\overline{v_1}$ of the horizontal sections of A, we can see that

$$v_2(A) = \overline{\nu_1}(A) - \overline{\nu_1}(A \ominus |),$$

where $A \ominus |$ stands for the Minkowski substraction of A by the unit vertical segment.

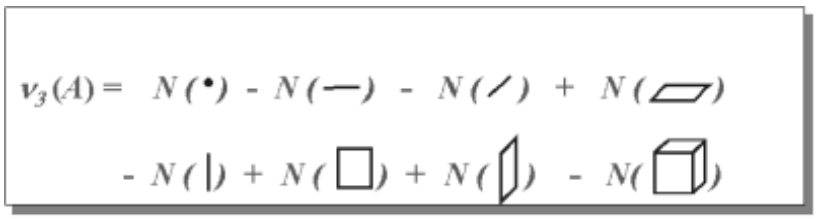

Figure 1.4: Euler-Poincaré Constant in R^3

In Z^3, this is the same, and Euler's number $v_3(A)$ defined as

$$v_3(A) = N\,(\text{vertices}) - N\,(\text{edges}) + N\,(\text{faces}) - N\,(\text{blocks})$$

is expressed by the same increment as before, for

$$v_3(A) = \overline{v_2}(A) - \overline{v_2}(A \ominus |) \tag{1.4}$$

when $\overline{v_2}(A)$ is the sum of Euler bidimensional numbers of the horizontal sections of A, and where $\ominus$ stands for he Minkowski substraction of A by the unit vertical segment (equation (1.4) can easily be extended to R^n by recurrence). Constant v_3 is independent of the choice of the "vertical" direction.

From an experimental point of view, the equation (1.4) is very convenient, for in image processing systems, Euler bidimensional constants are generally rapid to get and the unit linear erosion between two consecutive planes is a simple operation too. It is this equation (1.4) that has been implemented in the shinbone example below.

Finally, remember that the EPC of a simply connected object (i.e. homeomorphic to a cube) equals 1, that of a torus (typically, a donut) equals 0, and that of spherical crown (such as a football) equals 2. Moreover, the constant v is C-additive, which means that

$$v(A) + v(A') = v(A \cup A') + v(A \cap A'),$$

an equation that allows one to reduce complex figures to the most simple ones. Thus, the ECPC of lampshade pierced by 1000 pin holes equals -1000.

The topological number ν allows to bridge the gap between Euclidean and digital spaces, since it can be equivalently defined in both modes when

we interpret it in terms of graphs. Here, a convenient set model is the class of all finite unions of compact convex sets. This class, called "the convex ring of R^n" allows to elaborate a theory about measurements (Hadwiger theorem below), and on the other hand lends itself to digitization. In this framework, a deep property of Euler-Poincaré number is stated by the following theorem [14].

Theorem 1.1 *(Hadwiger): the only functional defined on the convex ring in R^n, of degree zero, invariant under displacements, C-additive and constant for the compact convex sets, is the Euler-Poincaré number ν.*

Note that unlike the number of particles, number ν is a local *measurement*: one needs only small neighborhoods around best points to estimate it statistically.

1.5.3 Minkowski measures

Euler-Poincaré number, that we have just introduced in the three-dimensional cases, is indeed defined by induction in any R^k. In particular:

- for $k = 0$, the space is reduced to one point and $\nu_0(X) = 1$ iff X is this point;

- for $k = 1$, $\nu_1(X)$ equals the number of segments of X;

- for $k = 2$, $\nu_2(X)$ equals the number of particles of X minus their holes.

Consider now a 3-D Euclidean set X, and a subspace $S(x, \omega)$ of location x and orientation ω. Take the cross section $X \cap S(x, \omega)$ and integrate its ν_k-constant over the displacements, i.e. in x and in ω. According to Hadwiger's theorem, we then obtain the only functionals to be invariant under

displacements, c-additive, homogeneous of degree $n - k$, and continuous for the compact convex sets, namely (up to a multiplicative constant):

$$\textit{volume} \qquad v(X) = \int_{\mathsf{R}^3} \nu_0 \left(X \cap \{x\}\right) \, dx \tag{1.5}$$

$$\textit{surface area} \quad \frac{1}{4} s(X) = \frac{1}{4\pi} \int_{4\pi} d\omega \int_{\pi\omega} \nu_1 \left[X \cap \Delta(x, \omega)\right] \, dx \tag{1.6}$$

$$\textit{mean caliper} \quad d(X) = \frac{1}{4\pi} d\omega \int_{4\pi} d\omega \int_{-\infty}^{+\infty} \nu_2 \left[X \cap \Pi(x, \omega)\right] \, dx \tag{1.7}$$

At first glance, the notation seems heavy; in fact, it is extremely meaningful. In Eq.(1.6) for example, ω indicates a direction on the unit sphere, and $\Delta(x,\omega)$ a test line of direction ω passing through point x. The first sum integrates over a plane Π_ω, orthogonal as ω, as the foot x of $\Delta(x,\omega)$ spans Π_ω. The second integral, in $d\omega$ is nothing but a rotation averaging (similar comment for Eq (1.7)). The meaning of these relations is clearly stereological. For example, the surface area, a 3-D concept, turns out to reduce to a sum of number of intercepts, i.e. a typically 1-D notion.

When set X admits at each point of its surface a mean curvature C and a total curvature C', then mean caliper and Euler-Poincaré number take another geometric interpretation, since

$$2\pi d(X) = \int_{\delta X} C\ ds \qquad \text{and} \qquad 4\pi\nu_3(X) = \int_{\delta X} C'\ ds$$

The three relations Eq.(1.5) to Eq.(1.7) attribute a *Euclidean* meaning to *digital* data (we meet again the turning point aspect of space graphs). By discretization, Eq.(1.5) becomes

$$v^*(X) = (\text{Number of voxels of } X) \times v_0$$

where $v_0 = a^3$ (cubic grid) or $a^{3/4}$ (fcc grid) or $a^{3/2}$ (cc grid).
Similarly, Eq.(1.6) is written

$$s^*(X) = (\text{average number of intercepts}) \times 2a^2\sqrt{2}$$

where the averaging is taken over the six directions of Eq.(1.2), in the cubic grid. Since estimate $s^*(X)$ concerns the Euclidean surface $s(X)$, it differs from the facets areas of the digital set X. For example, here, a facet of a zero thickness counts twice.

1.5.4 Other measurements

Being stereological is not an exclusive property of Minkowski functionals. Here are two instructive counter examples.

Roughness: Assume that δX admits curvatures everywhere, and let $F(l)$ be the combined chord distribution of X and X^c. Then, near the origin we have [27]

$$F(l) = \frac{l^2}{16}\left[-C' + 3\int_{\delta X} C^2 ds\right]$$

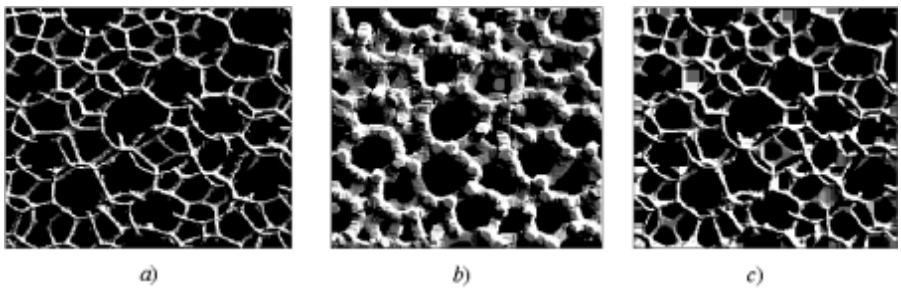

Figure 1.5: expanded polystyrene (foam); b) Cube-octahedral dilation of size 5 of a); c) Cube-octahedral closing of size 12 of a).

In particular, when X is a physical relief, the term C' vanishes, and the slope of the intercepts density near the origin is proportional to the average of the square mean curvature C^2. It was taken advantage of this descriptor to study road surfaces from profiles.

3-D contacts: Consider a random packing of spheres of radius R, and a cross section through it. The spheres becomes discs, and the distribution of the shortest distances between discs follows a law

$$F(l) \simeq 1.438 \quad n_c(lR)^{1/2}$$

where n_c is the number of contacts between spheres per unit volume [25]. This law, which governs some modes of thermic and electric permeabilities, has been experimentally verified [4].

Both above measurements are invariant under displacement, homogeneous, continuous on convex sets, but, unlike Minkowski functional, do not fulfill the c-additivity condition

$$\mu\left(X \cup X\right) + \mu\left(X \cap X'\right) = \mu\left(X\right) + \mu\left(X'\right),$$

which is not essential here.

1.5.5 Morphological mappings

As soon as spheres and lines (in a set of directions) are digitally defined, it becomes easy to implement linear and isotropic dilations and erosions.

Starting, for example, from the voxels of a cubic grid, one easily builds linear structuring elements with equidistributed directions : it suffices to take their common origin at the centre of a cube and the extremities at the middles of the faces (6 directions), or on the vertices (8 directions), or at the middles of the edges (12 directions).

Apart from linear structuring elements, the most commonly used are the spherical ones. This implies the datum of a metric. Between the cubic one, which is coarse and anisotropic, and the digital simulation of the Euclidean distance, which is the most elegant solution, but whose implementation is relatively complex, we choose here the cube-octahedric metric, for the reasons which have been discussed above (the readers interested by the digital approximations of the Euclidean distance may consult P.E. Danielsson [9], who proposes a sequential algorithm, P. Soille [32], who gives an implementation using queues of voxels, or Ch. Gratin and F. Meyer [12], who use hierarchical queues, see also [6] and [24]).

All usual isotropic 3-D dilations, erosions and filters derive from suprema and infima taken over the unit cube octahedron (as described in fig.(1.3), and from their iterations. The example presented in fig.(1.5) illustrates this point, by showing cube-octahedral dilation and closing of foam plastic.Two other views of initial polystyrene (a) are shown in fig.(1.6).

The 3-D reconstructions, binary and numerical ones, are carried out in the same way, and their uses are the same as in two dimensions, i.e. individual analysis, holes filling, connected granulometries, etc ... (for binary images), and extrema extraction, filtering by dynamics, swamping (for grey tone images). One of the major problems we meet here is the display of the objects under study, and we shall devote the next chapter to approach this goal by means of geodesic dilations, by using the intermediary steps involved in opening by reconstruction.

1.5.6 Watersheds and segmentation

The concept of a watershed is the same as in two dimensions, although its level by level implementation is fastiduous and often replaced by algorithms based on hierarchical queues [12][13]....

The most popular of these 3-D watersheds is that of the opposite $-dist_x$ of the distance functions of a set X, which allows to *segment* the set X under study into its major units. We will illustrate this segmenting technique by taking again the foam plastic example. This foam is obtained by expanding polystyrene, which produces polyhedral pores. If the expansion is too weak,

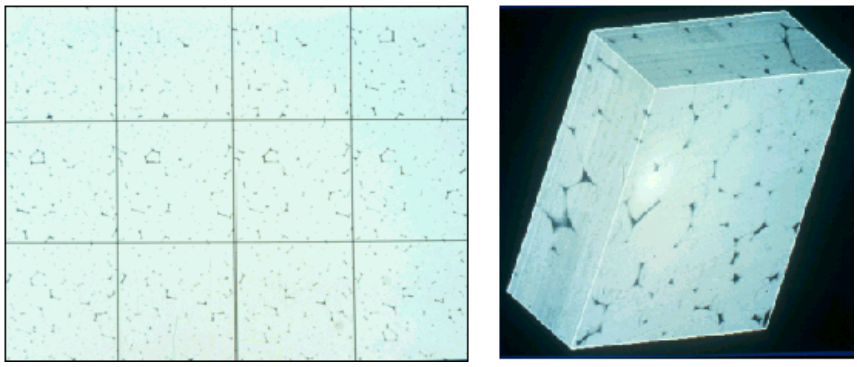

Figure 1.6: Series of cross sections and perspective view of foam plastic.

it does not yield elasticity, if it is too strong, the final product breaks up. The morphologist is therefore asked to describe the degree of "polyhedrization" of the foam, or more precisely of its complement. Now, the information contained in each individual 2-D section is obviously insufficient (see fig. ...), so that the pseudo cells must be individualized by a 3-D approach. The three steps of the process are then the following :

i/ computation of the 3-D distance function $-dist_x$ of the foam pores X;

ii/ reconstruction closing of $-dist_x$ by dynamics, in order to remove the non significant minima;

iii/ 3-D watershed Y of the filtered function.

The watershed surface Y delineates the separations between foam pores, that now appear as metallic grains in a solid volume (fig.1.7). A perspective view of the initial set is provided by fig.1.6, where the polyhedra turn out to be just sketched.We see how much the watershed reveals the underlying structure. The power of such a processing is more manifest again on cross sections.

How could it be possible to elaborate the segmentation shown in fig.1.7, from the small doted segments of fig.1.6, without an incursion in the 3-D space ?

1.5.7 Skeletons

The usefulness of skeletons and thinning operators, unlike that of whatersheds, seems rather problematic. Firstly, though the definition of a skeleton

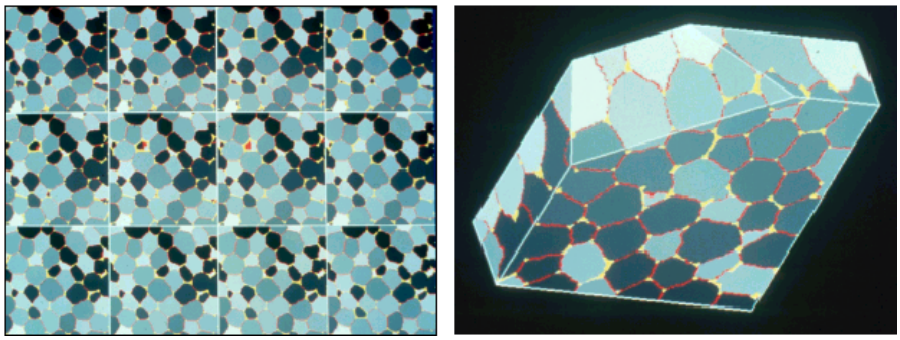

Figure 1.7: Series of cross sections and perspective view of the foam, after segmentation of the porous medium by watersheding

remains valid in three dimensions (i.e. locus of the centres of the maximal balls included in the set), the reality to which it refers is less simple, and comprises both medial lines and medial veils. Secondly, the pertinence of homotopy, as a topological descriptor ($\sim$ path equivalence) is unconfirmed. For example, there are two classes of equivalent paths in a disc with an internal hole, but one class only in a ball with a lacuna, such as a spherical crown.

Here, new classes of equivalence, holding on veils homeomorphic to the unit square, should be introduced, in addition to the path equivalence of usual homotopy. But even in the framework of the classical homotopy, another trouble arises, due to a combinatorial explosion : the 64 possible neighbourhoods of the unit hexagon, in the 2-D grid, become 4 096 for the cube-octahedron, and $2^{26} = 67\ 108\ 864$ for the unit digital cube! If 3-D homotopy appeals to some readers, they can consult the comprehensive survey of P.P. Jonker and A.M. Vossepoel [18] for the cubic case, or that of P. Bhanu Prasad and J.P. Jernot[5] for the cube-octahedral one.

Personally, we prefer to conclude this section, and the chapter, by showing an example of skeletonization. It is due to S. Bouchet [7], who uses, and improves, and algorithm initially proposed by Ch. Gratin [13]. Observing that the skeleton of a 3-D set is nothing but the crest surface of its quench function (in the sense of sect. 9-2), Ch. Gratin considers a drop of rain falling on the 3-D graph of the quench function at point $x \in \mathsf{R}^3$. The drop goes down to the lowest neighbour of x, y say. In the overall process,

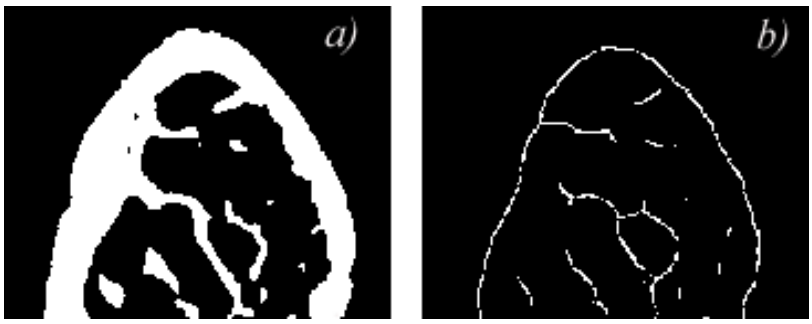

Figure 1.8: 2-D section of a mousse bone and of its 3-D skeleton.

the only voxels that do not receive water from upstream are those of the crest surface. Such an algorithm, easy to implement, results in acceptable skeletons, i.e. with relatively few barbs, but is has no particular reason to preverse homotopy.

The perspective view of fig.(1.9, a) is the binary image of mouse bone, obtained by microtomography. This specimen is made of 512 x 512 x 512 voxels, and one would like to describe the thicknesses of the bone walls. For answering the question, S. Bouchet proposes to compute the histogram of the quench function of the bone. Indeed, this quench function is a sort of diameter associated with all points of the 3-D skeleton. Therefore, it has a 3-D meaning, and weigths the various walls according to the extension of their medial surface, which seems reasonable.

The skeletonization is shown in fig.(1.8), via the display of a cross section, before (a) and after (b) the process. One can remark that some white particles are disconnected (lack of homotopy), others are clustered (3-D action), and that small holes do not enlarge (3-D lacunae). The histogramm of the quench function for the whole bone is given in fig.(1.9, b). The first mode corresponds to the fine walls in the centre of the bone, and the second mode to the thickness of the external envelope.

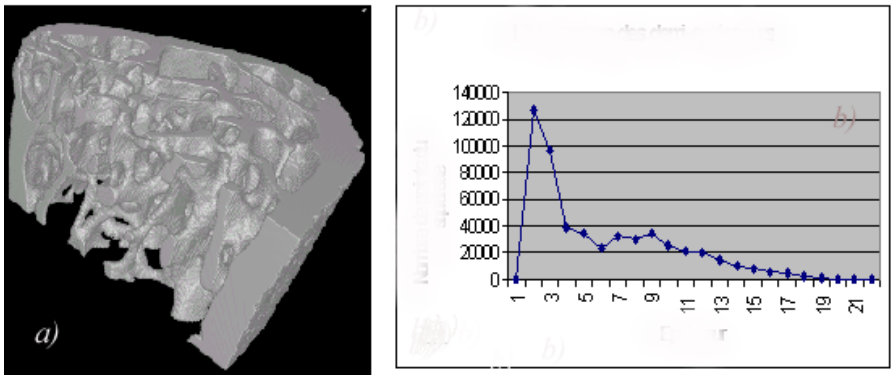

Figure 1.9: Pespective view of the bone (a), and histogramm of its quench function (b).

.

.

Chapter 2

3-D Geodesy and Segmentation

2.1 Geodesy and three-dimensional vision

In this chapter, we would like to show how 3-D geodesy enables us to "see" the binary structures in three dimensions. For human vision, the main difference between planar and three-dimensional sets is that we do not see the latter, but only their perspective projections, whereas the 2-D sets are integraly surveyed. Of course, we can make the perspective directions vary, move and turn the objects, but that does not allow to penetrate their interiors.

Now if we interpret a geodesic marker M as a point of view, and its increasing geodesic dilations inside a given set A as a progressive discovery, of even display, of the set, we get in hand a substitute for the perspective vision. It will be something else, different and with other advantages and disadvantages : we will be able to focus on internal branchings and necks in complex structures for exemple, or even to count correctly a number of holes.

Theoretically speaking, geodesy in three dimensions brings nothing really new into play, and from the algorithmic point of view, requires uniquely the choice of a digital unit ball. In the following we take the unit cube-octahedron, preferably to the cube, because it is more isotropic, but above all because its smaller size (13 voxels versus 27) allows us a finer description of the medium under study.

Since the problems treated below do not derive from new theoretical developments, it seems more appropriate to present them by means of two

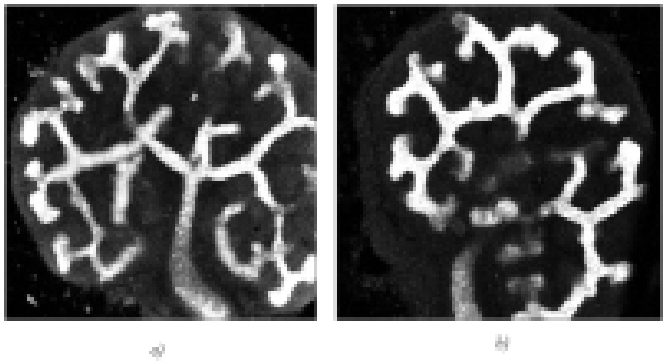

Figure 2.1: a) Kidney under study (supremum of the sections); b) other kidney specimen.

case studies, possibly accompanied by theoretical comments (specially at the end of the chapter, about the convenient metrics). The two examples used here were born from experience, more precisely from two separate issues in three-dimensional optical microscopy.

2.1.1 1st issue : the kidney

In February 2000, Dr. John Bertram[1], nephrologist and serving Chairman of the International Society for Stereology, spent two days at the CMM, during which he presented his current work. The subject of his research is the embryonic development of the kidney studied in animals such as the rat. He takes advantage of the property of embryonic kidney to develop in vitro, which enables him to study the organ evolution by confocal microscopy without animal destruction.[3].

Dr. Bertram left us the serial sections of two kidneys, and proposed to work with a student from the Ecole des Mines, for developing a morphological approach to his problem. Hence the decision to launch an internship for Gabriel Fricout.

We can see in figure(2.1) an image of each kidney after binarization, showing that the structure develops in the form of a tree. The expected

[1]Dpt of Anatomy, faculty of Medecine, Univ. de Melbourne, Parleville, Victoria 3052, Australia

morphological description bears on the geometry of the tree, and involves two objects :

- *extremities* : where are they located ? how are they arranged in space ?

- *branches* : where are they located ? according to which hierarchy and length ?

Confocal microscopy results in a highly anisotropic sample. Each series contains 29 sections 30 μ thick ; in which the orientation is roughly perpendicular to the trunk.

On each section, the pixels are arranged according to a square grid, whose spacing is about 4μ. The digital volume element (voxel) looks like a cylinder with a square base, which is seven times as high as it is wide. Each branch extremity is surrounded by nephrons, whose number is indicative of the future capacity of the fully-grown kidney. The nephrons, which cannot be seen here, will become visible through a future double staining. Then, we will have to study the relationship between the shape of the tree and the number of nephrons it can receive.

The discussion that followed Dr Bertram's talk showed that F.Meyer, S.Beucher and me did agree on ovoiding 3-D skeletons, and on approaching the problem by means of 3-D geodesy. Nevertheless, the student adopted a skeleton based method, but in 2-D, and associated with a 3-D back projection [10], i.e. a tailor-made approach for the images under study. However, when the shinbone problem arose, one month later, it became obvious that 3-D geodesy only could provide a general framework

2.1.2 2nd issue : the shinbone

Dr. Staub[2] studies the morphogenesis of long bones, and works on the shinbones of chicken embryos. He designed a dynamic model of the long central zone (shaft), where the compact future bone appears as a series of nested co-axial cylinders[34] (see figure 2.2). For verifying the model, an experiment conducted by M. Mendjeli has consisted in slicing the shinbone shaft, perpendicularly to its axis, into a series of a hundred semi-thin sections, roughly like slicing a sausage. It results into a nearly cubic grid of voxels whose step is close to the *micron* and whose size is approximately 300 x 300 x 100.

Unlike the previous example, the primary difficulty here is to detect the object under study. The nested cylinders are not directly visible, and one has no idea of the number of gaps and holes they may contain. However,

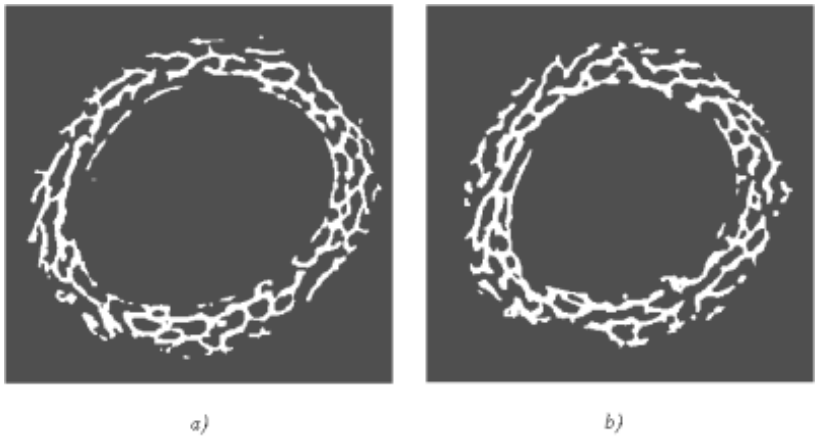

Figure 2.2: Two horizontal sections of a shinbone epiphysis

the bone image is virtually binary. Finally, as in the preceding example, the space is "oriented" from a marker : here the central marrow space ; there, the contact zone between the kidney and the gelatine (bottom of the tree).

Is it possible to segment the concentric cylinders of the bone, and to describe them in quantitative terms (thickness, porosity, contacts between cylinders, etc ...)?

2.2 Method : wavefronts

2.2.1 Wavefronts and tree diagrams

Let Z be a compact set in R^n and $x \in Z$, be a point in Z. The vawefront from a point x at distance λ is the geodesic sphere $F(\lambda, x)$ of (geodesic) radius λ and centered in x, where geodesy is generated by field Z.We propose to study the evolution of the connected components number of the wavefront $F(\lambda, x)$ when, as λ increases, the compact space Z is swept. The two types of branching, division or confluence, supposedly remain in finite number when $\lambda \in [0, \lambda_{\max}]$, so that for any branching at $\lambda = \lambda_0 < \lambda_{\max}$, it is always possible to find an open interval $]\lambda_1, \lambda_2[$ containing λ_0, and inside which there are no other branching. The number of branches which may gather in λ_0 is supposed to be finite. Finally, as the branching may take the two dual

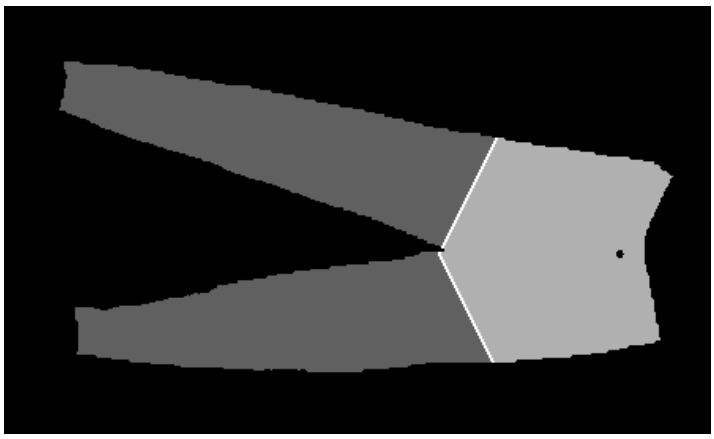

Figure 2.3: Example of branching

shapes (division or confluence) when λ increases, it is conventionally agreed in the proof below that the passage $\lambda_1 \rightarrow \lambda_2$ corresponds to a division

Therefore, we are led to the situation described in figure(2.3), where point x is in black, the ball $\overset{\circ}{B}(\lambda_0, x)$ in light grey, its complement $K(\lambda_0)$ in Z in dark grey, and where the white wavefront indicates the precise moment of the branching. So, the compact set

$$K(\lambda) = Z \backslash \overset{\circ}{B}(\lambda, x)$$

has a unique connected component, when $\lambda < \lambda_0$, and more when $\lambda > \lambda_0$. In order to determine what happens when $\lambda = \lambda_0$, we first observe that for compact sets, we have $\cap \{K(\lambda), \lambda < \lambda_0\} = K(\lambda_0)$.

The compact $K(\lambda_0)$ is composed of only one connected component. Otherwise, they would be separated by a minimum distance d ; but this is incompatible with the fact that, for any dilation of size ε, with $0 < \varepsilon < d$, the geodesic dilate of $K(\lambda_0)$ becomes connected. Therefore, the front $F(\lambda_0, x)$ itself is connected, as otherwise, to switch from one of its components to another one, it would be necessary to cross a $K(\lambda)$ with $\lambda > \lambda_0$, but these $K(\lambda)$ are not connected anymore.

When Z has several branchings, the same description applies for each branch, upwards or downwards from the propagation from point x, which consequently partitions the set Z into a series of successive pieces.

The case of the X branching has also to be considered. It occurs when at least two branches stop at the critical front, and at least two of them start from there. In this case, the intermediary connected region is reduced to the front in λ_0, for, if it was larger, we would come back to the previous case; and if the front was not taken into accout, we would no longer have a critical element, but only separated branches. By gathering these results, we can state :

Proposition 2.1 *Let Z be a compact of R^n. If, for any point $x \in Z$, the wavefront $F(\lambda, x)$ emanating from x admits a finite number of connected components, with a finite variation, then, as radius λ varies, $F(\lambda, x)$ partitions Z into a finite number of connected sections, corresponding to open intervals of λ, and separated by connected components of the front which are located at the critical points of the branchings.*

Clearly, the mapping $x \to P(x)$ which associates with any point $x \in Z$ the tree diagram characterized by the proposition, depends on the choice of point x, even if, when considering the common meaning of a tree, the partition remains almost the same for all the points selected low enough in the trunk. Besides, in this case, the tree may be defined as a partition for which there is no confluence for a suitably selected origin x (i.e. in the trunk).

Note that we are talking about connectivity here, and not about homotopy: in R^3 particularly, the sections may show closed pores or toric holes.

2.2.2 The ultimate elements of the wavefronts

This section takes up a classical C. Lantuejoul's and S. Beucher's result [20], but presents it differently. When using geodesics, it becomes possible to associate any point $x \in Z, Z \in \mathsf{R}^n$, with the point or points $y \in Z$ which are the furthest away from x. Indeed, let $\overset{\circ}{B}(\lambda, x)$ be the geodesic open ball of radius λ and centre x, and $\lambda_0$be the upper limit of the λ such that $\overset{\circ}{B}(\lambda, x)$ be strictly contained in Z. As the non empty compact sets $\left\{Z \backslash \overset{\circ}{B}(\lambda, x), \lambda < \lambda_0\right\}$ decrease and that R^n is a separated space, the intersection

$$x < \lambda_0 \cap \left[Z \backslash \overset{\circ}{B}(\lambda, x)\right] \tag{2.1}$$

is itself a non empty compact set, whose points are all at the maximum distance λ_0 from x. This intersection is named "geodesic ultimate eroded set", and $\overset{\circ}{B}(\lambda_0, x)$ is the "geodesic ultimate dilated set" of point x.

The existence of extreme points may also be considered in a regional framework, and not a global one anymore. We must suppose that, Z and x being given, it is possible to find a $\mu(Z,x) \leq \lambda_0(Z,x)$ such that each connected component of $Z \setminus \overset{\circ}{B}(\lambda, x), \mu \leqslant \lambda \leqslant \lambda_0$ decreases without subdividing. Then, the previous analysis should simply be applied to sets

$$K_i \cap \left[Z \setminus \overset{\circ}{B}(\lambda, x)\right] \qquad \mu \leqslant \lambda \leqslant \lambda_0$$

where the $K_i, i \in I$ refers to the connected components of $Z \setminus \overset{\circ}{B}(\mu, x)$. Therefore, we obtain the farthest connected components from point x, such as, for instance, the fingers tips for x taken around the middle of the wrist.

Both algorithm families about geodesics correspond to both our points of view. Invasion by geodesic balls led to all the particles reconstruction variants (deletion of the grains crossing the field border, hole filling, individual analysis, etc ...) and the search for extreme residues led to the ultimate eroded points, to the objects limits and to the length of a connected component (as a supremum of the distances between pairs of extreme points).

2.2.3 3-D Digital wavefronts

The digitization of geodesic operations may cause errors, but limited ones ; indeed, it is advisable to choose, as a circle or unit sphere, the closest shapes to their Euclidean homologues. Therefore, in 2D the hexagon, whose six vertices are equidistant from the center is better than the square, and, for the same reason, the cube-octahedron is better than the cube in 3D.

This Z^3 ball is very easy to build, when a numerical data network in square grid [30] is available. It suffices to shift all even planes by half a diagonal of the unit cube (any diagonal, but always the same one). In practice, data are of course not moved, but only structuring elements. For example, the substitute for the 13 vertices of the regular cube-octahedron of fig.(2.4) is calculated by dilating the central point according to the staggered unit cube-octahedron presented in the previous chapter (which differs whether the center lies in an even plane or in an odd one). The wavefront emanating

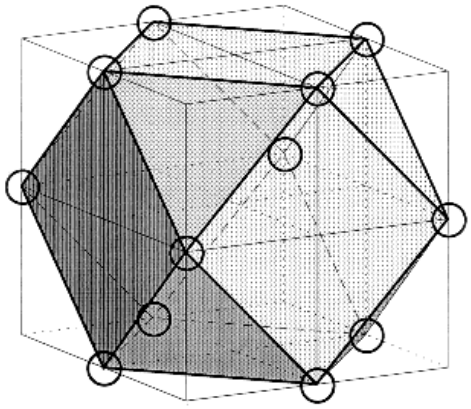

Figure 2.4: Cube-octahedron

from this central point starts with the point 12 neighbours ; when the inter-plane equals $a/\sqrt{2}$ (a = square grid spacing of the horizontal planes), the structure becomes completly isotropic and the 12 neighbours are equidistant from the center. This will be our assumption (section 4) about the shinbone, but this hypothesis is not essential, and, in any case, cannot be ventured for the study about embryonic kidneys (section 3)

The switch from the unit ball $C(x)$ of Z^3 (octahedron, prism or cube) to its geodesic version $B_1(x)$ inside a mask Z is

$$B_1(x) = C\,(x) \cap Z$$

and the geodesic ball $B_x\,(x)$ of the size is obtained by n iterations of the previous one :

$$B_n\,(x) = B_1\,[B_{n-1}\,(x)] \cap Z$$

The corresponding wavefront, or geodesic *sphere* equals

$$F_n\,(x) = B_{n+1}\,(x) \setminus B_n\,(x)$$

2.3 Use of the tree diagram for embryonic kidneys

In order to illustrate the above matter, we propose to segment the first one of the two kidneys of fig. 2.1. The analysis contains four steps :

1/ set construction from the initial data ;

2/ geodesic distance function of a marker in the set;

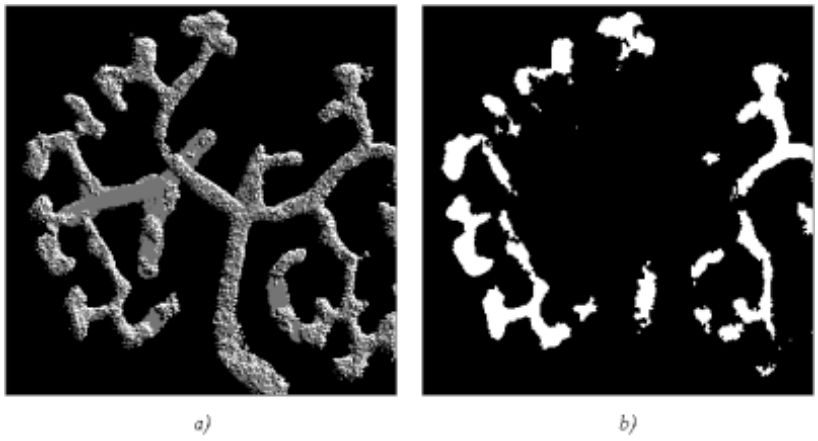

Figure 2.5: a) Perspective view of the binarized kidney; b) confocal section n]0xb014

3/ extremities;
4/ branches.

2.3.1 Binarization

This simple operation only requires a thresholding between 60 and 255, followed with the fill-in of the bi-dimensional internal pores. Still, the main connected component has to be extracted. In order to do this, we take as marker x one point at the beginning of the trunk. The reconstruction shows that the kidney tree diagram is broken around the middle in two separated parts. This is caused by the inaccuracy of confocal microscopy. In order to put it right, both parts have been reconnected by a small closing (see fig.(2.5a)).

2.3.2 geodesic distance function

The geodesic distance function starts from marker x at the base of the kidney and progresses inside the tree according to unit cube-octahedra (fig.2.6).

Figure 2.6: Geodesic distance function from the anchorage point (negative view of the supremum of the sections)

2.3.3 Extremities

The extremities are nothing but the region maxima of the previous geodesic function. These ultimate eroded points are shown on 2.7a, where lots of quite insignificant but very small real maxima can been observed. They are removed by a small surface opening (fig.2.7b). When using this algorithm in routinely, it would better to start with a regularization of the set under study by means of an isotropic tridimensional opening of size 1 or 2, providing that it does not break the connectivity.

2.3.4 Branchings

The extraction of branchings, which is conceptually simple, may nevertheless lead to a appreciable computing time. Considering the quite visible structure of the projected tree, the algorithm used below is slightly less precise, but faster and easier to implement.

In a first step, bidimensional branchings on the tree projection are investigated, then, we get back to the 3D space by building vertical cylinders whose bases are located at the 2D branchings, and slightly dilated (size 2). Finally, we take the intersection between these cylinders and the 3D tree. The operation leads to fig.2.8.

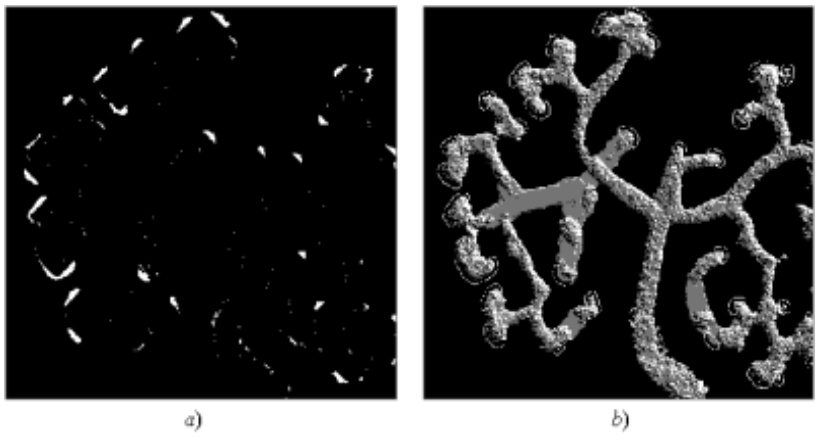

Figure 2.7: a) All extremities of the Kidney ; b) Filtered extremities.

Figure 2.8: Projection of the 3D branchings

2.3.5 Results

In all, starting from the connected kidney tree, we got to its segmentation into disjoint branches separated by thin branchings. Some branches contain one or more, of the tree extremities. From such a segmentation, it now becomes possible to replace the object under study by a "tree" in the meaning of graph theory, where the edges can be weighted geometrical characteristics (volume, length, location of its center, possible end points ... etc).

2.4 Shaft of chicken embryo shinbones

2.4.1 Purpose

The bone zone under study is situated in the central part of a chicken embryo shinbone, whose axis defines the vertical.The experimental data form a series of 98 rectangular slices of 320 x 310 pixels each. The uniform grey of the shinbone phase allowing an easy threshold (see fig.(2.9a)), the two problems to be solved are then the following :

1/ Implementing and checking Dr Staub's model, that is to say switching from the model of nested cylinders to an effective segmentation of the bone into nested structures thanks to some convenient quantitative criterion (to be found);

2/ Once the segmentation is achieved, extracting more specifically the bridges that link two successive cylinders, and calculating the homotopy of both bridges and cylinders.

2.4.2 Algorithm

For the sake of pedagogy, we work, on the one hand, on all 98 slices, and on the other hand, on the first 14 ones only. We call "bone" the first file, and "bone1" the second one. Thanks to reduced thickness file bone1, some structures are made more easily visible; moreover, the comparison between the wavefronts of bone and bone1 will inform us about the representativity of sample bone1.

If the nested cylinders model is correct, the wavefront stemming from the central medulla zone and penetrating into the bone should propagate more rapidly when it floods a cylindrical crown than when it crosses the narrow isthmuses that link the crowns altogether. Therefore, we have to :

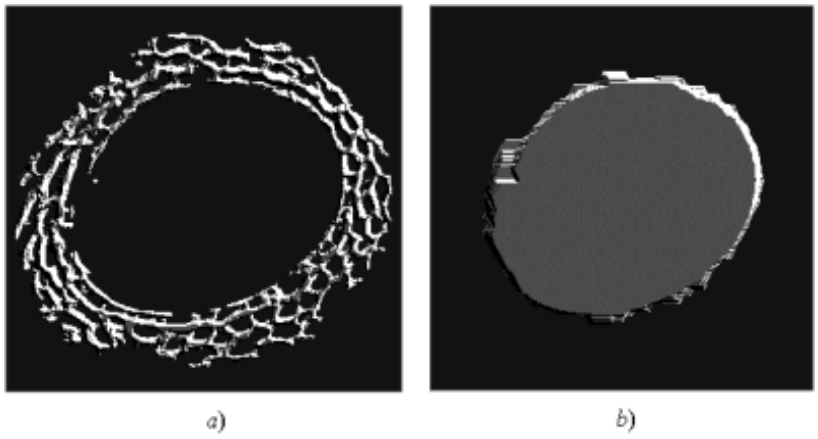

Figure 2.9: a) perspective view of bone1; b)Central cylindric marker M

- generate a relevant central marker M;
- plot the curve of the wavefront surface $F(\lambda, M)$ versus distance λ, which should show oscillations with more or less periodic minima ;
- decompose the geodesic wave into sections limited by minima values (bone segmentation);
- extract the wavefront at each minimum, which will result into bridges;
- calculate Euler constant for bridge sets, and cylinders;

... all operations that will now be executed.

2.4.3 Results

The central marker M is obtained by working one section after the other, and by extracting the central pore after opening (algorithm bone1), see fig.(2.9)b.

The measurement variation of the wavefront surface, for both files bone and bone1 is shown in fig.(2.10). Their minima are approximately on the same abcissae, for instance 16 instead of 13 or 6 instead of 5, which is an auspicious start.

Bone and bone1 segmentations, carried out from the following minima

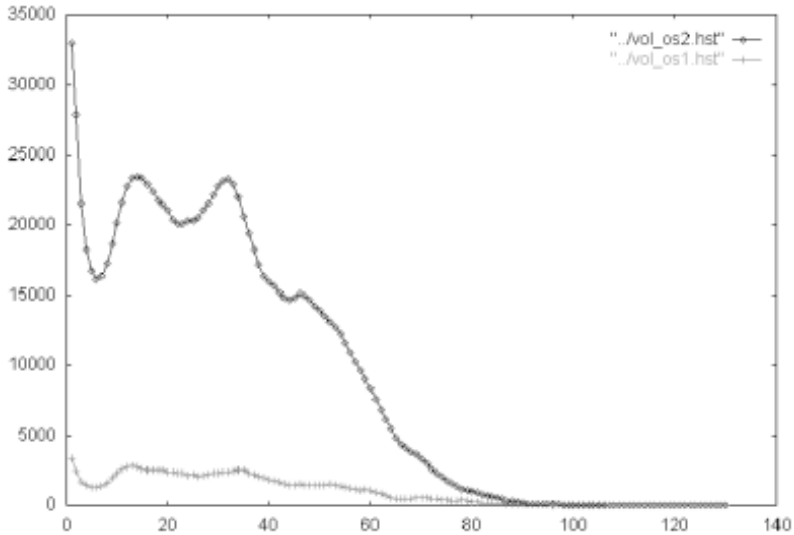

Figure 2.10: Plot of the wavefront surface versus the propagation steps

abcissae

$$6; 22; 44; \ldots\ldots\ldots\ldots\ldots\ldots\ldots\ldots \text{ for bone}$$
$$5; 18, 24; 41, 65; \ldots\ldots\ldots\ldots\ldots\ldots \text{ for bone1}$$

lead to the results shown on fig.(2.11).

In order to extract the branchings between cylinders, a stronger and partially false hypothesis has to be made: the wavefronts corresponding to each minimum of the plot are supposed to be exclusively located in these narrows. Based on this approximation, the bridges between cylinders i and $i+1$ match with the set difference between the m + 1 and m sized-geodesic dilates, where m is the abcissa of a minimum. On figure2.12, the contact zones between the first two cylinders are shown, for the files bone and bone1.

We now treat the last point, about countings on the various extracted sets. As one can note on the following table, the bone is quite pierced and broken.

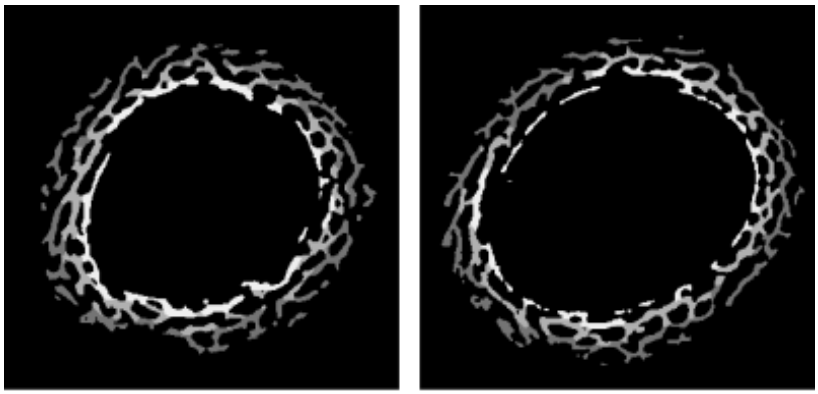

a) b)

Figure 2.11: 3D segmentations of two slices.

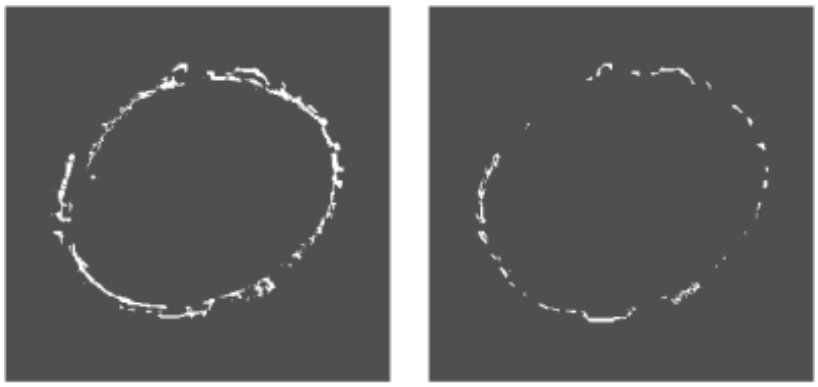

a) b)

Figure 2.12: Perspective views of the dilated bridges, for "bone" and "bone 1"

Region	*Euler Poincaré number*	
	bone	*bone1*
initial bone	*- 1 536*	*- 237*
connected component, adjacent to the marker	*- 1 885*	*- 275*
bridges between the first two cylinders	*1 447*	*205*
same bridges, followed by a unit dilation	*32*	*10*

Broken, for when reducing the object to its part adjacent to the central marker, at least 1885 - 1 536 = 349 small isolated parts are removed (experimental artifacts ?). Pierced, for this main connected component has 1885 holes, if it is admitted that it does not contains internal closed pores (this seems realistic when we consider the thicknesses).

The EPC of the bridges (1447) seems quite high. In fact, more than a nut linking one cylinder to the following one, a joint rather looks like a bundle of fine fibers. This is the reason why an elementary dilation (the 13 voxels of the unit cube-octahedron brings Euler-Poincaré number 1 447 down to 32.

2.5 Digital Geodesic Metrics

In both examples, we decided to start from digital metrics, those whose balls are the cube-octahedron of Z^3. Then, we considered the cube-octahedra $\mathrm{B}_1(x)$ centered in $x, \in \mathsf{Z}^3$, and with a size 1 as the structuring elements, and we have used their successive iterations to generate the wavefronts. Finally, we have considered the wavefronts as the spheres in a new metric, named geodesics, thanks to the Choquet theorem.

Meanwhile, we have surreptitiously replaced the metric balls with a set of dilations when time came to implement the first ones. Are these two notions equivalent ? Is it sufficient that the δ_λ increase with the positive parameter λ ? This is what we are going to study now. Indeed, for being able to build wavefronts, the data of a prior metric is a necessary but insufficient condition. We must also make sure that any point of the space remains accessible from any other one by a series of arbirary small dilations, namely, in the digital case, of the unit size. In other words, we must have

$$\delta_n = (\delta_1)^n$$

One can prove that in the digital cases, this condition, which is equivalent to the semi-group relation $\delta_\gamma \delta_\mu = \delta_{\lambda+\mu}$ is also sufficient. A number of families $\{\delta_\lambda\}$ can be built, that can satisfy it. Here are a few, in two or three dimensions. It is reminded that $\delta_1(x)$ can change its shape from one point to another one.

Metrics of regular lattices : those are precisely the ones where $\delta_1(x)$ shape does not change, i.e. which are translation invariant on a a regular grid, such as,

in Z^2 the symmetrical unit square of 9 or 5 points (diamonds), or the 7 point hexagon.

in Z^3 cube (27 points), the hexagonal basis-cylinder (21 points) or the cube-octahedron (13 points), the last one being the finest and the most isotropic.

geodesic metrics of a first mask : In practice, the previous metrics are only useful when the studied object is contained in a rectangular mask, Z say, which does not happen very often. Most of the time, on the contrary, the mask has cut out a region in a wider field, and, in order to manage this border effect, $\delta_1(x)$ is replaced by $\delta_1(x) \cap Z$. The same construction is correct when Z is an arbitrary given set, as the examples of sections 3 and 5 have shown. Besides, iterating a first geodesic used as an initial metric, in order to build a second one, is not forbiden.

Non unit dilations : Let us consider now as a unit ball the dilate δ_n of size n of the unit isotropic dilation of the grid, i.e.the square 3 x 3, or the 13 voxels cube-octahedron, for instance. The procedure consists of changing the connection, by replacing arcwise connectivity by that of the δ_n. It means that the component containing a given point x is not a one piece object anymore, but a group of objects whose dilate by δ_n is in one piece.

This non unit geodesics may save considerable time in 3-dimensionsal processes. Suppose for example we want to extract the arcwise connected component A_x at point x of a given set A. We can begin by eroding A by δ_n, then reconstruct it w.r. to the unit ball δ_n, and ending the process by geodesic dilations according to the unit ball δ_1. For large diameters of A compared to n, the computing time is asymptotically divided by n.

Sections and projections : As we have seen before about the kidney branchings, the projection of the stack of sections pile projection normally

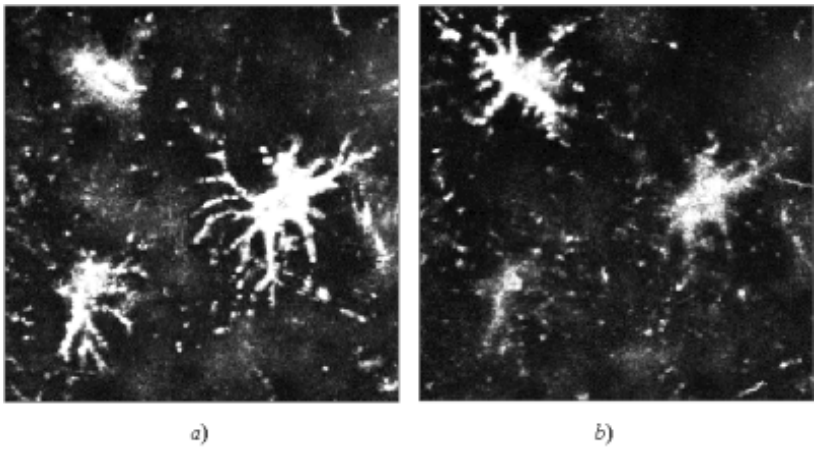

Figure 2.13: Sections numbers 15 (a), and 35 (b), from a stack of 57 confocal sections of osteocytes.

to their plane may be used as a basis for a tridimensional analysis. Consider for example a 3-D set A (in R^2or in Z^2), of connected component $\gamma_x(A)$ at point x. Let A_0 and x_0 be the projections of A and x respectively on a horizontal plane subspace.Then the vertical cylinder of basis the connected component of A_0 (in the 2-D sense) that includes x_0 contains $\gamma_x(A)$. Such a property allows an easy extraction of $\gamma_x(A)$, specially when the connected components of A are rather well separated.Beyond projection procedures, here again, it is not difficult to find non unit dilations and the accompanying connections. But in this case, only vertically aligned points can be gathered.

The following example illustrates this projection technique.The sequence under study comprises 57 8-bit digital images of 512 x 512 pixels. They come from a bone tissue, examined by confocal microscopy, with a one micron digital spacing. In this small volume of bone, we can see three osteocytes which are located at various depths. On both slices of fig.(2.13), the nuclei appear, as well as portions of long fibers of cytoplasm, that we are about to segment.

By taking the supremum of the 57 slices (fig.(2.14)a) and filtering them, we keep the three largest projections only (fig.(2.14)b) where the three disjoint connected projections of the osteocytes are visible. Consider the ver-

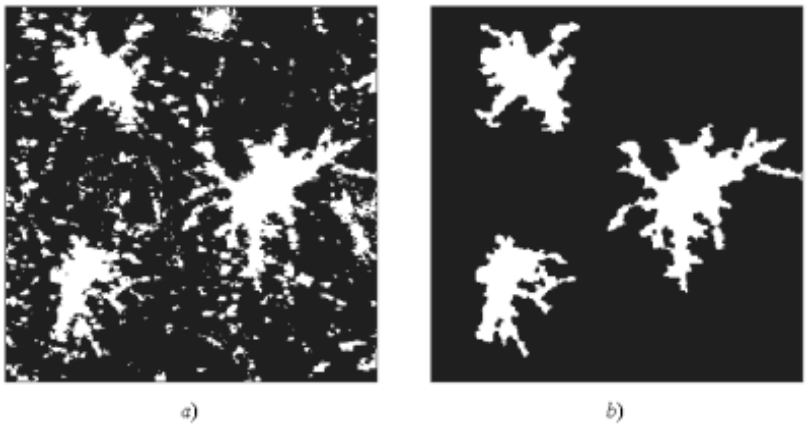

Figure 2.14: a) Threshold version of the supremum ; b) Extraction of the three largest objects.

tical cylinders with these projections as the bases, and restrict each of 57 sections to the inside of the cylinders. This results in figure (2.15), that shows a perspective view of the extracted cells.

In geodesic terms, these operations are equivalent to geodesic dilations by a vertical segment, taken as the unit dilating ball. This segment size is not one, but about fifteen points (otherwise, the whole cylinder could not be found). Then, only objects whose vertical dilate is arcwise-connected are considered connected, which finally yields the three largest cels of the stack.

2.6 Conclusion

Remarkably, the same wavefront concept in R^n or Z^n allows one to describe:

- the connected components,via its surface measurement;
- the bottlenecks, via the minima of its variation;
- the branches, via the variation of its connectivity;
- and the extremities, via through its ultimate locations;

and its application to complex 3-D histologic structures proves the outstanding power of this tool.

From a theoretical point of view, the wavefront properties bridge the three concepts of connection, metrics and dilation. An additive semi-group

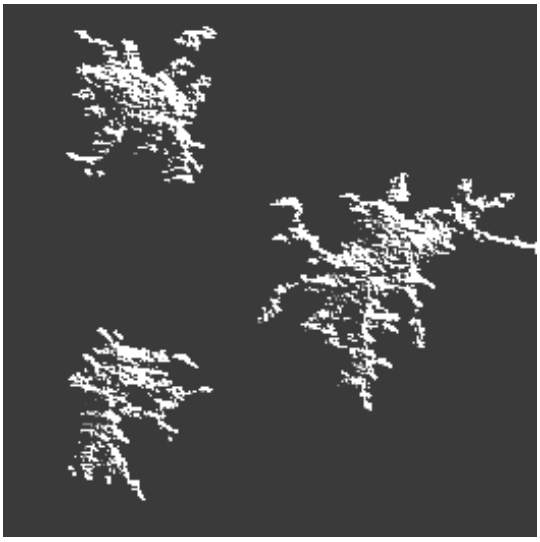

Figure 2.15: Perspective view of the extracted oesteocytes

of dilations is equivalent to a metric that admits geodesics, as well as to the compact connected components of a connection. This double equivalence opens the door to an a-priori infinite number of possibilities ; in fact, it seems up to now that connections by dilation are the only ones to have proved their practical usefulness.

Bibliography

[1] **G. Bertrand**, "Simple points, topological numbers and geodesic neighborhoods in cubic grids", *Pattern Rec. Letters*, vol. 15, pp. 1003-1012, 1994.

[2] **G. Bertrand** New Notions for Discrete Topology, in *Discrete Geometry for Computer Imagery*, Bertrand G.,Couperie M., Perroton L.(Eds.) Lecture notes in computer sciences, Vol 1568, Springer, 1999

[3] **A.T.Clark, R.J. Young and J.F. Bertram** . In vitro studies on the roles of transforming growth factor-beta1 in rat metaphrenic development, *Kidney Int* 59 pp 1641-1653 (2001).

[4] **P. Bhanu Prasad, J.P. Jernot, M. Coster, J.L. Chermant**, "Analyse morphologique tridimensionnelle des matériaux condensés", *in Proc. PIXIM,* 1988, pp. 31-42.

[5] **P. Bhanu Prasad, J.P. Jernot** Three dimensional homotopic thinning of digitized sets, *Acta Stereologica,* vol. 9, pp. 235-241, 1990

[6] **G.Borgefors** Distance transformations in digital space. *Computer Vision, Graphics and Image Porcessing*, vol 34, pp.344-37,1986.

[7] **S. Bouchet** Segmentation et quantification d'images tridimensionnelles. Techn. Report. Ecole des Mines de Paris, June 1999,102 p.

[8] **G. Choquet** *Topologie* Academic Press, N.Y. 1966.

[9] **P.E.Danielsson**, Euclidean distance mapping *Computer Graphics and Image Processing,* (1980)14, 227-248.

[10] **G.Fricout, L.A.Cullen-Mc Ewen, I.A. Harper , D.Jeulin , J.F. Bertram** A quantitative method for analysing 3D branching in embryonic kidneys:

[11] S. **Gesbert, C.V. Howard, D. Jeulin and F. Meyer,** "The use of basic morphological operations for 3D biological image analysis", *Trans. Roy. Microsc. Soc.*, vol. 1, pp. 293-296, 1990.

[12] **C. Gratin and F. Meyer**, "Mathematical Morphology in three dimensions", *Acta Stereol.* vol. 11, pp. 551-558, 1991.

[13] **C. Gratin**, *De la représentation des images en traitement morphologique d'images tridimensionnelles,* PhD thesis, Ecole des Mines de Paris, 1993, 200 p.

[14] **H. Hadwiger**, *Vorsesungen über Inhalt, Oberfläche und Isoperimetrie,* Springer, 1957.

[15] **V.C. Howard and K. Sandau**, "Measuring the surface area of a cell by the method of the spatial grid with a CSLM", *J. of Micr.,* vol. 165, pp. 183-188, 1992.

[16] **James and James**, *Mathematics Dictionary,* Van Nostrand, 1982.

[17] **P.P. Jonker**, "Parallel processing in computer vision and collision free path planning of autonomous systems", in *26th ISATA*, 1993.

[18] **P.P. Jonker**, **A.M.Vossepoel** Mathematical morphology for 3D images : comparing 2D and 3D skeletonization algorithms, *Summer School on morphological image and signal processing* Delft University, 1995.

[19] **T. Kong and A. Rosenfeld**, "Digital topology: Introduction and survey", *Comp. Vis. Image Proc.*, vol. 48, pp. 357-393, 1984.

[20] **C. Lantuejoul & S. Beucher,** On the use of geodesic metric in image analysis, *J. of microscopy,* 121, pp 39–49, 1981.6.

[21] **F. Meyer,** "Mathematical Morphology: from two dimensions to three dimensions", *J. of Micr.,* vol. 165, pp. 5-29, 1992.

[22] **J.C. Mullikin**, *Discrete and Continuous Methods for Three Dimensional Image Analysis*, Delft: Univ. Press, 1993.

[23] **J. Mukkerjee and B.N. Chatterji**, "Segmentation of three-dimensional surfaces", *Pattern Rec. Letters*, vol. 11, pp. 215-223, 1990.

[24] **N. Nikolaidis & I. Pitas,** *3-D Image Processing Algorithms*, Wiley , 2001, 176 p.

[25] **Y. Pomeau and J. Serra**, "Contacts in random packings of spheres", *J. of Micr.*, vol. 138, pp. 179-187, 1985.

[26] **J. Serra,** *Image analysis and mathematical morphology,* Academic Press, London, 1982.

[27] **J. Serra**, "Descriptors of flatness and roughness", *J. of Micr.*, vol. 134, pp. 227-243, 1984.

[28] **J. Serra,** *Image analysis and mathematical morphology, part II: theoretical advances,* J. Serra ed., Academic Press, London, 1988.

[29] **J. Serra**, "Mathematical Morphology for Boolean lattices", chapter 2 in *Image Analysis and Mathematical Morphology*, vol. 2, J. Serra (ed.), London: Acad. Press, 1988

[30] **J. Serra** Cube, cube-octahedron or rhombododecahedron as bases for 3-D shape descriptions", *Advances in Visual Form Analysis, C. Arcelli and Al. (eds.)* World Scientific 1997, 502-519.

[31] **J. Serra** Morphological descriptions using three-dimensional wavefronts (to be presented at *ISS'*2001,Bordeaux, France sept. 2001)

[32] **P. Soille** Spatial distributions from contour lines : an efficient methodology based on distance transformations, *Journal of Visual Communication and Image Representation* 2(2), (1991), 138-150.

[33] **P. Soille** *Morphologische Bildverarbeitung,* Springer, 1999, 316 p.

[34] **M. Staub** (personnal communication).

[35] **P.W. Verbeek, H.A. Vrooman and L.J. van Vliet**, "Low level image processing by max-min filters", *Signal Process.,* vol. 15, pp. 249-258, 1988.ASSP-34(4), pp. 898–911, August 1986.